Multifunctionality of particulate composites via cross-property maps

S. Torquato*
Department of Chemistry, Department of Physics, Princeton Institute for the Science and Technology of Materials, and Program in Applied and Computational Mathematics, Princeton University, Princeton, New Jersey 08544, USA

D. Chen
Department of Chemistry, Princeton University, Princeton, New Jersey 08544, USA

(Received 20 July 2018; published 26 September 2018)

Closed-form analytical expressions for the effective electrical (thermal) conductivity and elastic moduli of a wide class of three-dimensional isotropic particulate composites (dispersions) for all phase contrasts and volume fractions have been previously formulated. These property estimates were extracted from exact strong-contrast expansions that incorporate complete microstructural information. In this paper, we employ these analytical expressions to derive and apply "cross-property maps" that connect combinations of pairs of the aforementioned effective transport and elastic properties to one another for a wide class of dispersions in which the inclusions can have different shapes and sizes and are spatially distributed in a matrix with varying degrees of order/disorder. We illustrate cross-property maps for a variety of cases (e.g., incompressible or compressible composites with conducting/insulating inclusions that may be rigid or compliant or auxetic) for high inclusion volume fractions. All of the cross-property maps that involve the effective conductivity translate immediately into equivalent results for the effective dielectric constant, magnetic permeability, or diffusion coefficient because they are mathematically analogous. We discuss an example that enables us to design a disordered dispersion with desired values of the effective dielectric constant and effective Young's modulus. Cross-property maps and their extensions will facilitate the rational design of particulate media with different desirable multifunctional characteristics. Moreover, our investigation has implications for the application of machine-learning and other data-driven approaches for multifunctional materials discovery.

DOI: 10.1103/PhysRevMaterials.2.095603

I. INTRODUCTION

It is desirable to design materials with useful multifunctional characteristics, including transport, mechanical, electromagnetic, chemical, and flow properties. However, it is difficult to find homogeneous materials that possess these multifunctional characteristics. On the other hand, composite materials (mixtures of two or more materials) are ideally suited to achieve multifunctionality, since the best features of different materials can be combined to form a new material that has a broad spectrum of desired properties [1,2].

It is generally desired to design a composite material with N effective properties, which we denote $K_e^{(1)}, K_e^{(2)}, \ldots, K_e^{(N)}$, given the individual properties of the phases. In principle, one would like to know the region (set) in the multidimensional space of effective properties in which all composites must lie; see Fig. 1 for a schematic of the allowable region. The size and shape of this region depend on how much information about the microstructure is specified and on the prescribed phase properties. For example, the set over all volume fractions is clearly larger than the one in which the volume fractions are specified. Including even more information about the microstructure in the form of higher-order correlation functions [3] will reduce the set of possible composites even further. The determination of the allowable region is generally a highly complex problem. However, the identification of the allowable region can be greatly facilitated if cross-property bounds on the effective properties can be found. Cross-property bounds are inequalities that rigorously link different effective properties to one another [3]. For example, links between different transport properties [3–10] and between the conductivity and the elastic moduli [3,10–16] have been established. Cross-property bounds are especially useful in identifying the boundary of the allowable region (see Fig. 1) and hence the set of optimal multifunctional composites [1,17–20]. A technologically important subset of composite materials with desirable multifunctional characteristics is particulate media [3,21–28].

The main objective of this paper is to determine cross-property maps that connect combinations of pairs of effective electrical (or thermal) conductivity σ_e and elastic moduli, such as the effective Young's modulus E_e and Poisson's ratio ν_e, to one another for a wide class of isotropic particulate composites (dispersions). One could attempt to accomplish this goal via numerical methods (e.g., finite-element techniques) that solve the governing differential equations and then average the relevant fields to get the effective properties [3], but this is unwieldy due to fact that one must search an infinite parameter space (possible phase properties and microstructures). A far better solution is to derive analytical cross-property formulas, but this too is extremely challenging.

*torquato@princeton.edu

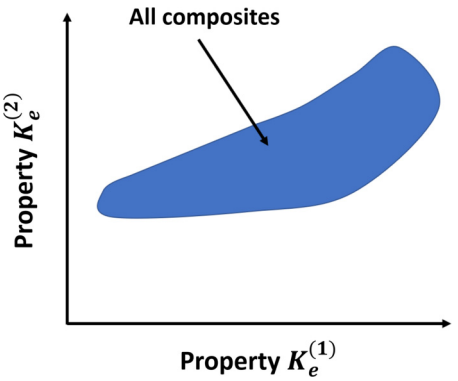

FIG. 1. Schematic illustrating the allowable region in which all composites with specified phase properties must lie for the case of two different effective properties. The locus of points on the boundary of the allowable region corresponds to the set of optimal multifunctional composites.

For this purpose, one might consider employing effective-medium or mean-field approximations that are based on exact single-inclusion boundary-value problems [29–32]. However, these approximations necessarily can account only for simple microstructural information, such as the volume fraction and inclusion shape. In fact, it is known that the effective properties generally depend on an infinite set of n-point correlation functions [33–39]. Thus, although mean-field approximations may sometimes provide qualitative trends on the behavior of the effective properties of some dispersions, they cannot be quantitatively predictive for general situations because they do not account for higher-order microstructural information [3].

For the problem at hand, we employ accurate microstructure-sensitive rational-function formulas for the effective conductivity [35] and effective elastic moduli [40] to derive cross-property maps that are applicable to a wide class of three-dimensional macroscopically isotropic particulate composites for all phase contrasts and volume fractions. These approximate relations for the effective properties of isotropic dispersions in any space dimension d were obtained by truncating corresponding exact strong-contrast series expansions after third-order terms but approximately account for complete microstructural information [35,38]; see Sec. II for the relevant formulas and ramifications for the present paper. They are given in terms of the phase properties, phase volume fractions, and functionals involving the three-point correlation function as embodied in two different three-point parameters: ζ_2 and η_2, as defined below. Since the exact series expressions perturb about the optimal Hashin-Shtrikman structures [41–44], these formulas have been shown to provide excellent estimates of the effective properties for a wide range of phase contrasts and volume fractions for a wide class of dispersions in which the inclusions are prevented from forming large clusters [35,40]. Moreover, they always lie within rigorous three-point or cross-property bounds and are superior to popular mean-field approximations. While these accurate approximations have been widely used to estimate individual effective transport or elastic properties for a diverse class of dispersions [45–51], they have heretofore not been applied to derive cross-property maps.

For reasons of mathematical analogy, the determination of the effective conductivity translates immediately into equivalent results for the effective dielectric constant, magnetic permeability, or diffusion coefficient [3]. Thus, any cross-property relations involving the dimensionless effective conductivity apply as well to these other mathematically analogous effective properties when made appropriately dimensionless.

We explicitly state the rational-function approximations for the effective conductivity and effective elastic moduli for three-dimensional dispersions in Sec. II. Since it is crucial to understand the class of dispersions for which these expressions are highly predictive, we provide the necessary theoretical background to elucidate their validity. In Sec. III, we determine cross-property maps between the effective conductivity and the effective moduli as well as between different independent effective elastic moduli for particulate media using combinations of these accurate approximation formulas. When the cross-property relations are sufficiently functionally simple, they are explicitly stated. Cross-property maps are graphically represented for a number of select examples. In Sec. IV, we describe how cross-property maps can aid in the rational design of multifunctional particulate composites with specified material components and volume fractions. Finally, we make concluding remarks, including implications for the use of machine-learning and other data-driven approaches to ascertain cross-property maps for general composites.

II. THEORETICAL BACKGROUND

Exact strong-contrast perturbation expansions for the effective conductivity tensor and stiffness tensor of macroscopically anisotropic composite media [52] in d-dimensional Euclidean space $\mathbb{R}^d$ consisting of two isotropic phases have been derived [37,38]. The nth-order tensor coefficients are given explicitly in terms of integrals over products of certain tensor fields and a determinant involving the set of n-point correlation functions $S_1^{(p)}, S_2^{(p)}, \ldots, S_n^{(p)}$ for phase p that systematically render the integrals absolutely convergent in the infinite-volume limit. The quantity $S_n^{(p)}(\mathbf{x}_1, \ldots, \mathbf{x}_n)$ gives the probability of finding n points with positions $\mathbf{x}_1, \ldots, \mathbf{x}_n$ in phase p (where $p = 1$ or 2). In the special case of macroscopically isotropic media, this d-dimensional strong-contrast expansion for the effective conductivity tensor reduces to the one originally derived by Torquato [35].

Another useful feature of these expansions (expressible in powers of the phase "polarizabilities") is that they converge rapidly for a class of dispersions for all volume fractions, even when the phase properties differ significantly. The reason for this is that the exact series expression can be regarded to be expansions that perturb about certain dispersions that realize the optimal two-point bounds [53] for macroscopically anisotropic media [3,54]. For macroscopically isotropic media, these optimal dispersions correspond to the Hashin-Shtrikman structures for the effective conductivity [41], effective bulk modulus K_e [42], and effective shear modulus G_e [43,44]. The structures that realize all of the optimal two-point bounds have the important topological/geometrical features

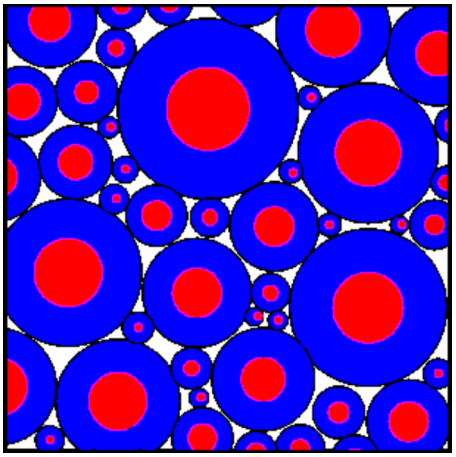

FIG. 2. Schematics of the coated-spheres model (as adapted from Ref. [3]) consisting of composite spheres that are composed of a spherical core of one phase (dispersed phase) that is surrounded by a concentric spherical shell of the other phase such that the fraction of space occupied by the core phase is equal to its overall phase volume fraction. The composite spheres fill all space, implying that there is a distribution in their sizes ranging to the infinitesimally small. Thus, the matrix (blue region) is a fully connected (continuous) phase and the inclusions (red regions) are well separated from one another.

that one phase is disconnected or dispersed in a special way (described below) and the other is a fully connected (continuous) matrix phase.

Figure 2 depicts a schematic of the coated-spheres model, which is optimal for the effective conductivity σ_e and effective bulk modulus K_e because they realize the corresponding two-point Hashin-Shtrikman bounds [3,41,42]. One can view the continuous matrix phase (blue region) as the most topologically connected phase with respect to the effective conductivity or effective bulk modulus. Moreover, the inclusions are geometrically restricted in that any pair of inclusions must be "well separated" from one another (except at the trivial volume fraction in which they fill all of space) due to the impenetrable concentric shells, whose thickness depends on the volume fraction. When the inclusions (red regions) constitute the more conducting or stiffer phase, the coated-spheres model exactly achieves the Hashin-Shtrikman lower bound on the effective conductivity or effective bulk modulus. When the inclusions constitute the more insulating or compliant phase, the coated-spheres model exactly achieves the Hashin-Shtrikman upper bound on the effective conductivity or effective bulk modulus.

A. Accurate approximations for the effective conductivity of particulate media

Henceforth, we focus on macroscopically isotropic two-phase media. Let us assume that phases 1 and 2 are the matrix and dispersed phases, respectively, of a dispersion. Truncation of the d-dimensional strong-contrast series expansion in Ref. [35] after third-order terms yields the expression

$$\frac{\sigma_e}{\sigma_1} = \frac{1 + (d-1)\phi_2\beta - (d-1)\phi_1\zeta_2\beta^2}{1 - \phi_2\beta - (d-1)\phi_1\zeta_2\beta^2}, \tag{1}$$

where

$$\beta = \frac{\sigma_2 - \sigma_1}{\sigma_2 + (d-1)\sigma_1} \tag{2}$$

and ζ_2 is a three-point parameter that depends on the space dimension d and must lie in the closed interval [0,1]. For $d = 3$, it is defined by the following threefold integral:

$$\zeta_2 = \frac{9}{2\phi_1\phi_2}\int_0^\infty \frac{dr}{r}\int_0^\infty \frac{ds}{s}\int_{-1}^1 d(\cos\theta)P_2(\cos\theta) \times \left[S_3^{(2)}(r,s,t) - \frac{S_2^{(2)}(r)S_2^{(2)}(s)}{\phi_2}\right], \tag{3}$$

where P_2 is the Legendre polynomials of order 2 and θ is the angle opposite the side of the triangle of length t.

Formula (1) was shown by Torquato [35] to give an *accurate approximation* of the effective conductivity of a wide class of d-dimensional dispersions for all volume fractions and all phase conductivities. This class of dispersions includes those in which the particles ("polarized" phase), generally, do not form *large clusters*. However, for the special case of bicontinuous porous media in which the void (polarized) phase is perfectly insulating ($\sigma_2 = 0$), approximation (1) may still provide a good estimate of σ_e. The reason for this is that the flux is carried by the *connected* solid (i.e., nonpolarized) phase, regardless of whether the void phase is connected or disconnected.

It is noteworthy that when $\zeta_2 = 0$, formula (1) is identical to the Hashin-Shtrikman lower bound on σ_e when $\sigma_2 \geqslant \sigma_1$ or the Hashin-Shtrikman upper bound σ_e when $\sigma_2 \leqslant \sigma_1$ [41] and hence to dispersions that realize them, such as the coated-spheres model depicted in Fig. 2. Therefore, dispersions for which ζ_2 deviates from 0 are those whose microstructures deviate from these optimal dispersions in which the inclusions are well separated from one another in a fully connected matrix. The three-point parameter $\zeta_2(\phi_2)$ is a monotonically increasing function of the inclusion volume fraction ϕ_2. For spherical inclusions of identical size or not, it is known that $\zeta_2 = 0$ in the limit $\phi_2 \to 0$ [55–57] and hence formula (1) is exact through first order in ϕ_2 [3]. For nonspherical inclusions, $\zeta_2 > 0$ in the limit $\phi_2 \to 0$ [3]. Deviations of ζ_2 from 0 at positive values of ϕ_2 can be induced by allowing the inclusions to get arbitrarily close to one another or have a nonspherical shape. Moreover, polydispersity in the size of the inclusions can still lead to values of ζ_2 that can deviate appreciably from 0 if the inclusions can get arbitrarily close to one another. To get a qualitative sense of how ζ_2 can vary across different microstructures, consider the four dispersions of nonoverlapping inclusions schematically illustrated in Fig. 3: ordered identical spheres (disks) [Fig. 3(a)], disordered identical spheres (disks) [Fig. 3(b)], disordered polydispersed spheres (disks) [Fig. 3(c)], and disordered identical ellipsoids (ellipses) with random orientations [Fig. 3(d)]. Based on the aforementioned considerations, at a fixed volume fraction and away from close-packed states, ζ_2 is smallest in Fig. 3(a) because the inclusions are spherical and well separated and is largest in Fig. 3(d) because the inclusions are nonspherical and are not well separated. The case in Fig. 3(b) shows a ζ_2 value that is generally larger than that for the case in Fig. 3(a) because the inclusions can get arbitrarily close to one another and yet is

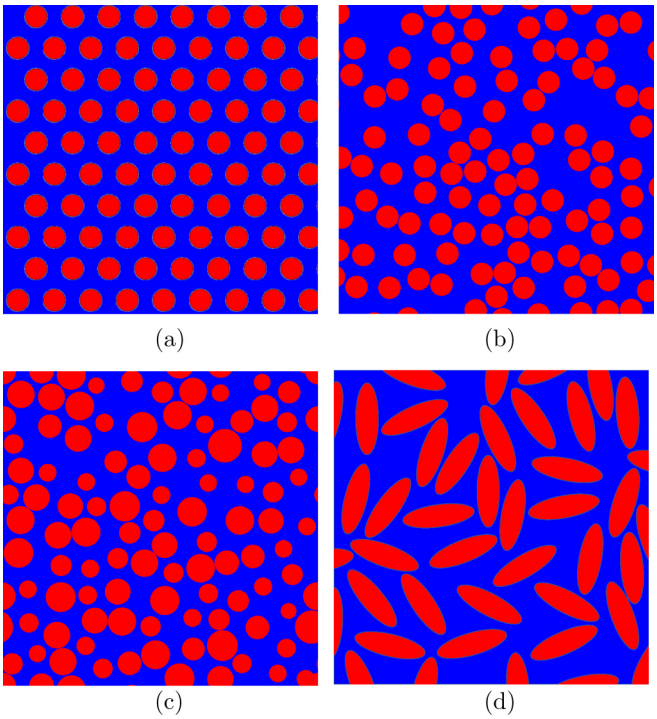

FIG. 3. Select representative examples of the wide class of dispersions of nonoverlapping inclusions in a matrix for which formulas (1), (5), and (6) and resulting cross-property relations apply. (a) Ordered dispersion of identical spheres (disks). (b) Disordered dispersion of identical spheres (disks). (c) Disordered dispersion of spheres (disks) of different sizes. (d) Disordered dispersion of identical ellipsoids (ellipses) with random orientations. At a fixed volume fraction and away from close-packed states, ζ_2 is generally smallest for (a), next smallest for (b), larger for (c), and largest for (d). Qualitatively, the same trends apply to the three-point parameter η_2 [3], which arises in rigorous three-point bounds on the effective shear modulus G_e as well as formula (6).

smaller than that for the case in Fig. 3(c) because in Fig. 3(c) they have a size distribution and also are not well separated. These trends are quantitatively supported by previous studies on the determination of ζ_2 for various dispersions [3]; see also a summary of some of these results for $d = 3$ in the Appendix.

For $d \geqslant 3$, formula (1) always lies between the best available rigorous upper and lower three-point bounds on σ_e [3], provided that

$$\zeta_2 \leqslant 1/(d-1). \tag{4}$$

Thus, formula (1) should be applied for $d = 3$ only when $\zeta_2 \leqslant 0.5$. It is noteworthy that for a wide class of models of random media, some of which are summarized in the Appendix, the parameter ζ_2 always meets this condition, and hence estimates based on (1) always lie between the tightest three-point bounds.

B. Accurate approximations for the effective elastic moduli of particulate media

Again, here we specialize to macroscopically isotropic elastic two-phase media, which are characterized by two independent effective elastic moduli, say the effective bulk modulus K_e and effective shear modulus G_e. Let phases 1 and 2 denote the matrix and dispersed phases, respectively. Truncation of the d-dimensional strong-contrast series expansions for K_e and G_e [38,39] after third-order terms for the special case $d = 3$ yields the following expressions:

$$\frac{K_e}{K_1} = \frac{1 + \frac{4G_1}{3K_1}\kappa\phi_2 - \frac{10G_1}{3(K_1+2G_1)}\kappa\mu\phi_1\zeta_2}{1 - \kappa\phi_2 - \frac{10G_1}{3(K_1+2G_1)}\kappa\mu\phi_1\zeta_2}, \tag{5}$$

$$\frac{G_e}{G_1} = \frac{1 + \frac{9K_1+8G_1}{6(K_1+2G_1)}\mu\phi_2 - \frac{2\kappa\mu G_1}{3(K_1+2G_1)}\phi_1\zeta_2 - \frac{\mu^2}{6}\gamma}{1 - \mu\phi_2 - \frac{2\kappa\mu G_1}{3(K_1+2G_1)}\phi_1\zeta_2 - \frac{\mu^2}{6}\gamma}, \tag{6}$$

where

$$\kappa = \frac{K_2 - K_1}{K_2 + \frac{4G_1}{3}}, \tag{7}$$

$$\mu = \frac{G_2 - G_1}{G_2 + G_1\left[\frac{9K_1+8G_1}{6(K_1+2G_1)}\right]}, \tag{8}$$

$$\gamma = \left[\frac{3K_1 + G_1}{K_1 + 2G_1}\right]^2 \phi_1\eta_2 + 5G_1\left[\frac{2K_1 + 3G_1}{(K_1 + 2G_1)^2}\right]\phi_1\zeta_2. \tag{9}$$

While the same three-point parameter ζ_2 defined by (3) arises in the expression for the effective bulk modulus, another three-point parameter, $\eta_2 \in [0, 1]$, is involved in the effective shear modulus, which is defined by the threefold integral

$$\eta_2 = \frac{5\zeta_2}{21} + \frac{150}{7\phi_1\phi_2}\int_0^\infty \frac{dr}{r}\int_0^\infty \frac{ds}{s}\int_{-1}^1 d(\cos\theta)P_4(\cos\theta) \times \left[S_3^{(2)}(r,s,t) - \frac{S_2^{(2)}(r)S_2^{(2)}(s)}{\phi_2}\right], \tag{10}$$

where P_4 is the Legendre polynomials of order 4 and θ is the angle opposite the side of the triangle of length t. The parameters ζ_2 and η_2 have also arisen in rigorous bounds on the effective moduli of three-dimensional composites [3,58–62] and have been computed for a variety of model dispersions; see Refs. [3] and [62].

When $\zeta_2 = 0$, formula (5) is identical to the Hashin-Shtrikman lower bound on K_e when $G_2 \geqslant G_1$ or to the Hashin-Shtrikman upper bound K_e when $G_2 \leqslant G_1$ [42] and hence to the optimal dispersions that realize them, such as the coated-spheres model depicted in Fig. 2. When $\zeta_2 = 0$ and $\eta_2 = 0$, formula (6) is identical to the Hashin-Shtrikman lower bound on G_e when $G_2 \geqslant G_1$ and $K_2 \geqslant K_1$ or the Hashin-Shtrikman upper bound K_e when $G_2 \leqslant G_1$ and $K_2 \leqslant K_1$ and hence to the optimal dispersions that realize them [43,44]. While the coated-spheres model does not achieve these bounds on G_e, they are still achieved by a class of microstructures in which one phase is a *disconnected, dispersed phase in a fully connected (continuous) matrix*. Qualitatively, the same trends described above for the values that ζ_2 can take for the wide class of dispersions considered here (see Fig. 3) apply as well to the three-point parameter η_2, as evidenced by results reported in previous investigations; see Ref. [3] and references therein as well as the Appendix here.

Formulas (5) and (6) were shown by Torquato [63] to yield accurate estimates of the effective bulk and shear moduli, respectively, of the aforementioned wide class of dispersions

for all volume fractions and phase properties, provided the particles generally do not form large clusters. When the dispersed phase is stiffer than the matrix, the third-order formulas mimic (to an excellent approximation) the behavior of *higher-order lower bounds* on the effective moduli. On the other hand, when the dispersed phase is more compliant than the matrix, the third-order formulas mimic (to an excellent approximation) the behavior of *higher-order upper bounds* on the effective moduli. It was required that the three-dimensional approximations (5) and (6) always lie within the most restrictive three-point upper and lower bounds [63]. This generally implies that intervals in which the geometrical parameters ζ_2 and η_2 lie will be more restrictive than the interval [0,1]. For example, for the three-dimensional effective bulk modulus formula, (5), it was shown that when $G_1/K_1 \leqslant 0.75$, then

$$\zeta_2 \leqslant 0.6 + \frac{8}{15}\frac{G_1}{K_1}, \tag{11}$$

in order for (5) to lie between the Beran-Molyneux bounds on the effective elastic moduli [58]. However, if $G_1/K_1 > 0.75$, then there is no additional restriction on ζ_2. Thus, the constraints on ζ_2 for (5) to obey the tightest three-point bounds on K_e are less restrictive than that for (1) to lie between the tightest three-point bounds on σ_e [cf. (4)]. Similarly, there are restrictions on the three-point parameter η_2 for (6) to lie between the tightest three-point bounds on G_e [63], but these are not presented here, since they have no bearing on the applications to dispersions that we focus on here. Indeed, for a number of realistic models of three-dimensional dispersions [3], the parameters ζ_2 and η_2 are such that the estimates from relations (5) and (6) always lie within the tightest three-point bounds.

III. CROSS-PROPERTY MAPS

In what follows, we ascertain cross-property maps between the effective conductivity and effective moduli as well as between different independent effective elastic moduli for three-dimensional particulate media using combinations of the accurate approximation formulas for the effective conductivity, (1) (with $d = 3$), effective bulk modulus, (5), and effective shear modulus, (6). We assume that the class of particulate media are characterized by three-point parameters under the relatively mild restriction that $\zeta_2 \leqslant \eta_2 \leqslant 1/2$, for reasons discussed in Sec. II. Under these assumptions, the key idea to get the desired cross-property maps is to eliminate both ζ_2 and η_2 from formulas (1), (5), and (6) to express one effective property in terms of another effective property and phase information (phase properties and volume fractions). Often, we express our results for the elastic moduli in terms of the effective Young's modulus E_e and effective Poisson's ratio ν_e, which are straightforward to measure experimentally and can be obtained from K_e and G_e via the following interrelations:

$$\frac{9}{E_e} = \frac{1}{K_e} + \frac{3}{G_e}, \tag{12}$$

$$\nu_e = \frac{3K_e - 2G_e}{2(3K_e + G_e)}. \tag{13}$$

In each case, we generally present three cross-property maps—$\sigma_e(E_e)$, $\sigma_e(\nu_e)$, and $\nu_e(E_e)$—which are given in terms of dimensionless units.

Because the parameter space is infinite, in much of the ensuing discussion, we examine special cases of relations (5) and (6) in which one or both of the phases have extreme values, e.g., $K_1/G_1 = \infty$, $K_2/G_2 = \infty$, $K_2/K_1 = G_2/G_1 = 0$ or ∞, and/or $\sigma_2/\sigma_1 = 0$ or ∞. Other nonextreme cases are examined as well. We focus on high inclusion volume fractions, namely, $\phi_2 = 0.4$, 0.5, and 0.6, which are also the most challenging cases to treat. The range of possible values of the different effective properties for each ϕ_2 spans realizable particulate media, which is determined by the possible values that the aforementioned microstructure-dependent parameter ζ_2 can take; the largest range occurs at the largest volume fraction, $\phi_2 = 0.6$. Specifically, based on previous determinations of the three-point parameters for a wide class of dispersions, we assume that $0 \leqslant \zeta_2 \leqslant 0.25$, $0 \leqslant \zeta_2 \leqslant 0.29$, and $0 \leqslant \zeta_2 \leqslant 0.33$ for $\phi_2 = 0.4$, 0.5, and 0.6, respectively; see Ref. [3] and the Appendix. The same restrictions apply to η_2, since we assume that $\zeta_2 \leqslant \eta_2$, as discussed above.

A. Incompressible composites with rigid, conducting inclusions

We first consider incompressible composites in which $\nu_1 = \nu_2 = 1/2$ (or $K_1/G_1 = K_2/G_2 = \infty$) that contain rigid, conducting inclusions. Materials that are effectively incompressible include elastomers and some metals, such as gold. It noteworthy that conductive elastomeric composites have been fabricated [64]. To begin, we consider superrigid ($G_2/G_1 = \infty$) and superconducting ($\sigma_2/\sigma_1 = \infty$) inclusions. For such incompressible particulate media, the cross-property relation between the effective conductivity σ_e and the effective Young's modulus E_e can be written in the simple closed form

$$\frac{\sigma_e}{\sigma_1} = \frac{\psi + \left(\frac{E_e}{E_1} - 1\right)6\beta\mu^2\phi_2}{\psi - \left(\frac{E_e}{E_1} - 1\right)3\beta\mu^2\phi_2}, \tag{14}$$

where

$$\mu \to \frac{G_2 - G_1}{G_2 + \frac{3}{2}G_1} = \frac{E_2 - E_1}{E_2 + \frac{3}{2}E_1}, \tag{15}$$

$$\psi = \beta^2(4 + 6\mu\phi_2) - 3\mu^2 + \frac{E_e}{E_1}[3\mu^2 + \beta^2(4\mu\phi_2 - 4)]. \tag{16}$$

When the inclusions are superrigid ($G_2/G_1 = \infty$) and superconducting ($\sigma_2/\sigma_1 = \infty$), the cross-property relation, (14), becomes

$$\frac{\sigma_e}{\sigma_1} = \frac{1 + \frac{E_e}{E_1}(10\phi_2 - 1)}{1 + 9\phi_2 - \frac{E_e}{E_1}\phi_1}. \tag{17}$$

The corresponding cross-property formula between the effective conductivity σ_e and the effective shear modulus G_e simply involves replacing E_e/E_1 in (17) with G_e/G_1. It is noteworthy that the determination of the effective shear modulus of such a dispersion is exactly equivalent to finding the effective viscosity of the dispersion in the *infinite-frequency* limit [3]

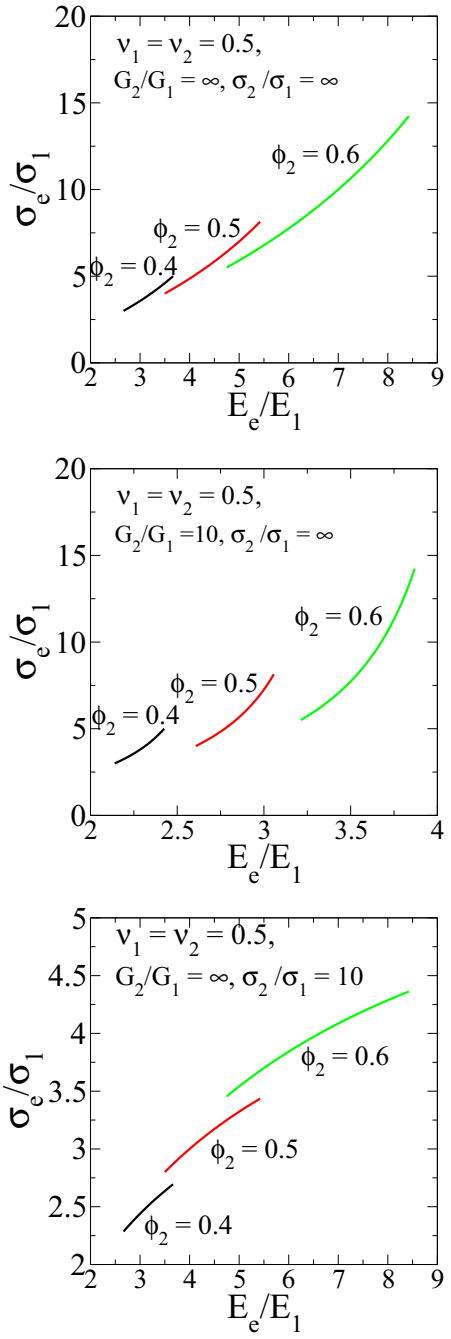

FIG. 4. Cross-property map $\sigma_e(E_e)$ for incompressible composites that contain rigid, conducting inclusions at select high values of the inclusion volume fraction ϕ_2. For a fixed value of ϕ_2, moving along any curve from left to right, ζ_2 increases from its minimum value of 0.

The topmost plot in Fig. 4 shows the cross-property map obtained from formula (17) for realizable dispersions for inclusion volume fractions $\phi_2 = 0.4$, 0.5, and 0.6. While the left end point for each of the three curves corresponds to $\zeta_2 = 0$ (Hashin-Shtrikman lower bound for σ_e and E_e), the right end point for each curve corresponds to the largest value of ζ_2 for the respective volume fraction. Thus, moving along the curves from left to right spans the possible types of microstructures, as schematically depicted in Fig. 3. As expected, the effective conductivity $\sigma_e(E_e)$ is a monotonically increasing function of E_e for fixed ϕ_2. This is because the particle phase is more conducting and stiffer than the matrix phase; as particles become closer to each other, the system deviates from the Hashin-Shtrikman lower bound and hence both σ_e and E_e increase. Moreover, for similar reasons, as ϕ_2 increases, both σ_e and E_e increase. To determine how sensitive these results are to changes in the ratio G_2/G_1 or σ_2/σ_1, we include cross-property maps in Fig. 4 for $G_2/G_1 = 10$ (all other phase contrast ratios are the same) and for $\sigma_2/\sigma_1 = 10$ (all other phase contrast ratios are the same), as obtained from the general incompressible formula, (14). We see that for the case $G_2/G_1 = 10$, the possible values and range of E_e/E_1 drop appreciably for each volume fraction. Similarly, for $\sigma_2/\sigma_1 = 10$, the possible values and range of σ_e/σ_1 drop appreciably for each volume fraction.

B. Incompressible composites with compliant, insulating inclusions

For incompressible composites ($\nu_1 = \nu_2 = 1/2$) that contain liquid inclusions ($G_2/G_1 = 0$) that are perfectly insulating ($\sigma_2/\sigma_1 = 0$), the cross-property relation, (14), becomes

$$\frac{\sigma_e}{\sigma_1} = \frac{\phi_1 + \frac{E_e}{E_1}(6\phi_2 - 1)}{1 + 5\phi_2 - \frac{E_e}{E_1}}. \tag{18}$$

The cross-property map obtained from this formula is plotted in the topmost panel in Fig. 5. While the left end point for each of the three curves corresponds to the largest value of ζ_2, the right end point for each curve corresponds to $\zeta_2 = 0$ (Hashin-Shtrikman upper bound for σ_e and E_e). Clearly, the effective conductivity $\sigma_e(E_e)$ is a monotonically increasing function of E_e for fixed ϕ_2. This is due to the fact that the particle phase is less conducting and more compliant than the matrix phase. As the particles become closer to each other, the system deviates from the Hashin-Shtrikman upper bound and hence both σ_e and E_e decrease. Moreover, for similar reasons, as ϕ_2 increases, both σ_e and E_e decrease, which is exactly opposite to the trend shown in Fig. 4. All other phase contrasts being equal, changing G_2/G_1 to 0.1 or changing σ_2/σ_1 to 0.1 results in cross-property maps that are significantly different from the topmost curve shown in Fig. 5, and these two cases are graphically represented in the middle and bottommost panels in Fig. 5, respectively. We see that for the case $G_2/G_1 = 0.1$, the possible values and range of E_e/E_1 increase appreciably for each volume fraction. Similarly, for $\sigma_2/\sigma_1 = 0.1$, the possible values and range of σ_e/σ_1 increase appreciably for each volume fraction.

C. Compressible matrix with rigid, conducting/insulating inclusions

Here we determine cross-property maps for compressible matrices ($\nu_1 < 1/2$) and superrigid ($G_2/G_1 = \infty$) inclusions that are either superconducting ($\sigma_2/\sigma_1 = \infty$) or perfectly insulating ($\sigma_2/\sigma_1 = 0$). Figure 6 shows the cross-property maps for compressible matrices with $\nu_1 = 0.29$ and superconducting inclusions for inclusion volume fractions $\phi_2 = 0.4$, 0.5, and 0.6. As expected, the effective conductivity $\sigma_e(E_e)$ is a monotonically increasing function of E_e, and $\sigma_e(\nu_e)$ a

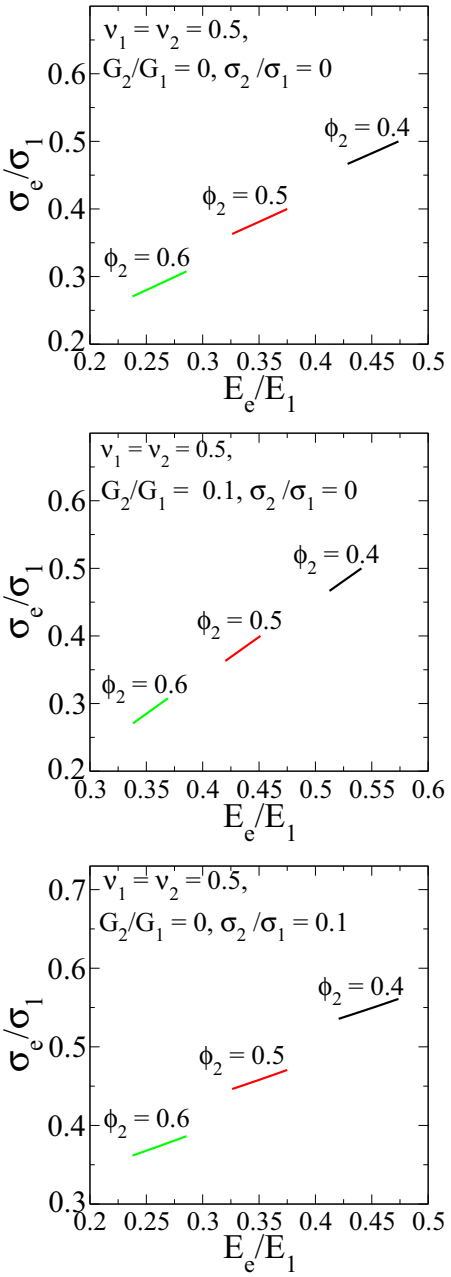

FIG. 5. Cross-property maps for $\sigma_e(E_e)$ for incompressible composites that contain compliant, insulating inclusions at select high values of the inclusion volume fraction ϕ_2. For a fixed value of ϕ_2, moving along a curve from right to left, ζ_2 increases from its minimum value of 0.

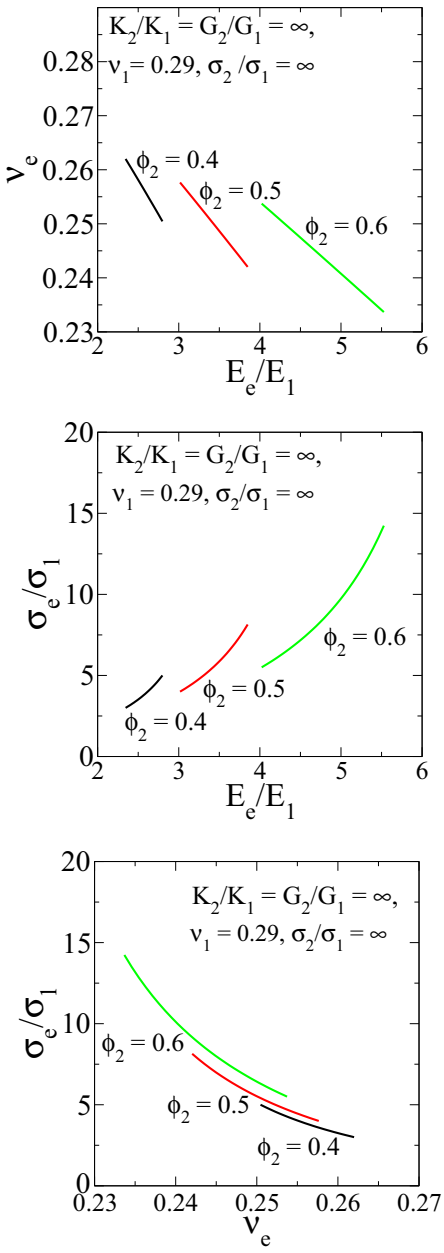

FIG. 6. Cross-property maps for $\nu_e(E_e)$ (top), $\sigma_e(E_e)$ (middle), and $\sigma_e(\nu_e)$ (bottom) for compressible matrices that contain rigid, conducting inclusions at select high values of the inclusion volume fraction ϕ_2. For either $\nu_e(E_e)$ or $\sigma_e(E_e)$ at fixed ϕ_2, moving along a curve from left to right, ζ_2 increases from its minimum value of 0. For $\sigma_e(\nu_e)$ at fixed ϕ_2, moving along a curve from right to left, ζ_2 increases from its minimum value of 0.

monotonically decreasing function of ν_e for fixed ϕ_2. The effective Poisson's ratio $\nu_e(E_e)$ is a monotonically decreasing function of E_e. This is for reasons similar to those mentioned in the cases above. The left end point of $\sigma_e(E_e)$ and $\nu_e(E_e)$ corresponds to $\zeta_2 = 0$ (Hashin-Shtrikman lower bound for E_e), and the right end point of $\sigma_e(E_e)$ and $\nu_e(E_e)$ corresponds to the largest value of ζ_2 for the respective ϕ_2. The left end point of $\sigma_e(\nu_e)$ corresponds to the largest value of ζ_2, and the right end point of $\sigma_e(\nu_e)$ corresponds to $\zeta_2 = 0$ (Hashin-Shtrikman lower bound for σ_e) for the respective ϕ_2.

Figure 7 shows the cross-property maps for compressible matrices with $\nu_1 = 0.29$ and insulating inclusions for inclusion volume fractions $\phi_2 = 0.4$, 0.5, and 0.6. The cross-property map $\nu_e(E_e)$ in this case is the same as the top curve in Fig. 6 and, thus, is not shown in Fig. 7. The effective conductivity $\sigma_e(E_e)$ is a monotonically decreasing function of E_e for fixed ϕ_2, and $\sigma_e(\nu_e)$ a monotonically increasing function of ν_e. The left end point of $\sigma_e(E_e)$ corresponds to $\zeta_2 = 0$ (Hashin-Shtrikman upper bound for σ_e), and the right end point of $\sigma_e(E_e)$ corresponds to the largest value of ζ_2 for

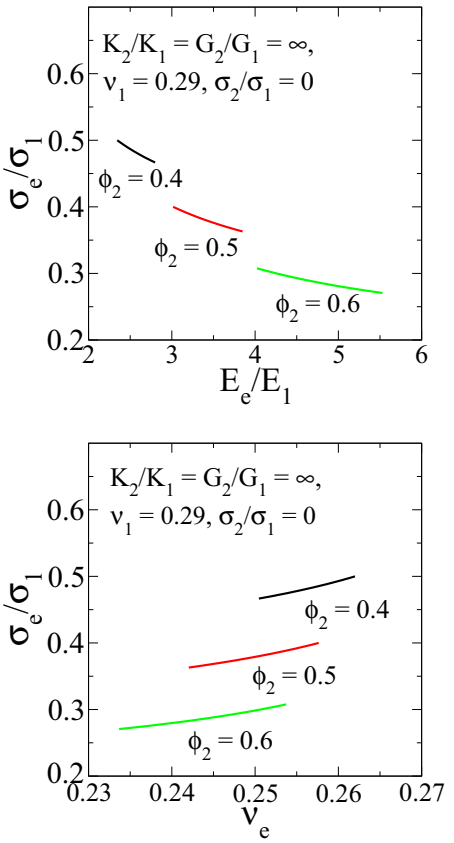

FIG. 7. Cross-property maps $\nu_e(E_e)$ (top), $\sigma_e(E_e)$ (middle), and $\sigma_e(\nu_e)$ (bottom) for compressible matrices that contain compliant, insulating inclusions at select high values of the inclusion volume fraction ϕ_2. For $\sigma_e(E_e)$ at fixed ϕ_2, moving along a curve from left to right, ζ_2 increases from its minimum value of 0. For $\sigma_e(\nu_e)$ at fixed ϕ_2, moving along a curve from right to left, ζ_2 increases from its minimum value of 0.

the respective ϕ_2. The left end point of $\sigma_e(\nu_e)$ corresponds to the largest value of ζ_2, and the right end point of $\sigma_e(\nu_e)$ corresponds to $\zeta_2 = 0$ (Hashin-Shtrikman upper bound for σ_e) for the respective ϕ_2.

D. Compressible matrix with conducting/insulating cavities

Here we determine cross-property maps for compressible matrices ($\nu_1 < 1/2$) and cavities ($K_2 = G_2 = 0$) that are either superconducting ($\sigma_2/\sigma_1 = \infty$) or perfectly insulating ($\sigma_2/\sigma_1 = 0$). We also examine how these results change when the matrix is incompressible.

Figure 8 shows the cross-property maps for compressible matrices with $\nu_1 = 0.29$ and superconducting cavities for inclusion volume fractions $\phi_2 = 0.4$, 0.5, and 0.6. The effective conductivity $\sigma_e(E_e)$ and $\sigma_e(\nu_e)$ are monotonically decreasing functions of E_e and ν_e for fixed ϕ_2, respectively, and the effective Poisson's ratio $\nu_e(E_e)$ a monotonically increasing function of E_e. The left end point of $\sigma_e(E_e)$ and $\sigma_e(\nu_e)$ corresponds to the largest value of ζ_2, and the right end point of $\sigma_e(E_e)$ and $\sigma_e(\nu_e)$ corresponds to $\zeta_2 = 0$ (Hashin-Shtrikman lower bound for σ_e) for the respective ϕ_2. The left end point of $\nu_e(E_e)$ corresponds to the largest value of ζ_2, and the right

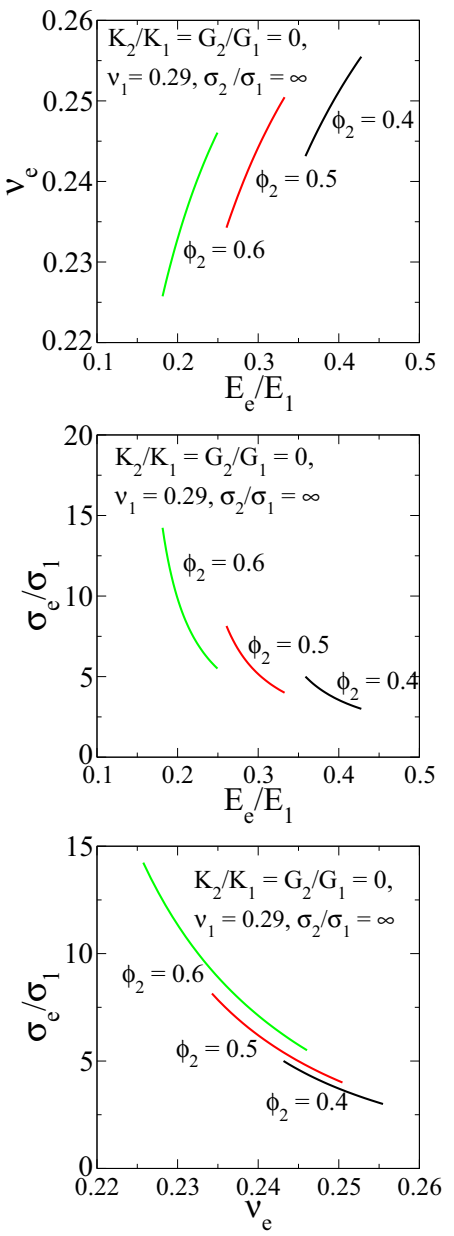

FIG. 8. Cross-property maps $\nu_e(E_e)$ (top), $\sigma_e(E_e)$ (middle), and $\sigma_e(\nu_e)$ (bottom) for compressible matrices that contain conducting cavities at select high values of the inclusion volume fraction ϕ_2. For fixed ϕ_2, moving along any curve from right to left, ζ_2 increases from its minimum value of 0.

end point of $\nu_e(E_e)$ corresponds to $\zeta_2 = 0$ (Hashin-Shtrikman upper bound for E_e) for the respective ϕ_2.

In the limit that the matrix becomes incompressible, i.e., $K_1/G_1 = \infty$ or $\nu_1 = 1/2$, the cross-property relations are particularly simple functionally and given by the following closed-form expressions:

$$\frac{\sigma_e}{\sigma_1} = \frac{3 - 12\phi_2 + \frac{G_e}{G_1}(10\phi_2 - 3)}{3\phi_1 + \frac{G_e}{G_1}(\phi_2 - 3)}, \tag{19}$$

$$\frac{\sigma_e}{\sigma_1} = \frac{\phi_1(2 - 20\phi_2) - 9\frac{K_e}{G_1}\phi_2}{2\phi_1(1 + 5\phi_2) - 9\frac{K_e}{G_1}\phi_2}, \tag{20}$$

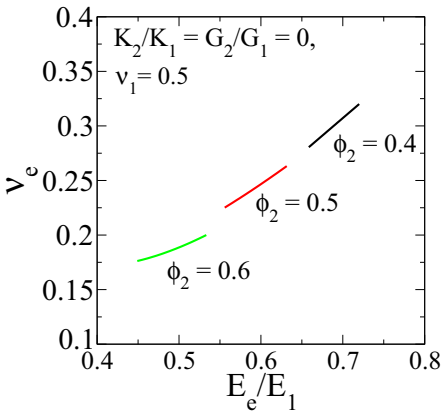

FIG. 9. Cross-property maps for $\nu_e(E_e)$ (top) for incompressible matrices that contain conducting cavities at select high values of the inclusion volume fraction ϕ_2. For fixed ϕ_2, moving along any curve from right to left, ζ_2 increases from its minimum value of 0.

and

$$\frac{G_e}{G_1} = \frac{12\phi_1(5\phi_2 - 2) - 27\frac{K_e}{G_1}\phi_2}{8\phi_1(5\phi_2 - 3) - 27\frac{K_e}{G_1}\phi_2}. \tag{21}$$

We note that we can also derive the cross-property maps $\sigma_e(E_e)$, $\sigma_e(\nu_e)$ and $\nu_e(E_e)$ analytically for this incompressible case; however, they are rather complicated functionally and hence we do not explicitly give them here. The cross-property map $\nu_e(E_e)$ for an incompressible matrix changes dramatically from the one shown in the topmost panel in Fig. 8 for a compressible matrix, as shown in Fig. 9. Since the effective conductivity σ_e does not change with ν_1, we do not provide plots of $\sigma_e(E_e)$ or $\sigma_e(\nu_e)$.

Figure 10 shows the cross-property maps $\sigma_e(E_e)$ and $\sigma_e(\nu_e)$ for a compressible matrix with $\nu_1 = 0.29$ and insulating cavities for inclusion volume fractions $\phi_2 = 0.4$, 0.5, and 0.6. The cross-property map $\nu_e(E_e)$ in this case is the same as the top curve in Fig. 8 and, thus, is not shown in Fig. 10. The effective conductivities $\sigma_e(E_e)$ and $\sigma_e(\nu_e)$ are monotonically increasing functions of E_e and ν_e for fixed ϕ_2, respectively. The left end point for each curve corresponds to the largest value of ζ_2, and the right end point corresponds to $\zeta_2 = 0$ (Hashin-Shtrikman upper bound for σ_e) for the respective ϕ_2.

In the limit that the matrices become incompressible, i.e., $K_1/G_1 = \infty$ or $\nu_1 = 1/2$, the cross-property relations are particularly simple functionally and given by the following closed-form expressions;

$$\frac{\sigma_e}{\sigma_1} = \frac{3\phi_1 + \frac{G_e}{G_1}(4\phi_2 - 3)}{3 + 6\phi_2 - \frac{G_e}{G_1}(5\phi_2 + 3)}, \tag{22}$$

$$\frac{\sigma_e}{\sigma_1} = \frac{\phi_1(28 - 40\phi_2) + 9\frac{K_e}{G_1}\phi_2}{\phi_1(28 + 20\phi_2) + 9\frac{K_e}{G_1}\phi_2}. \tag{23}$$

The cross-property maps $\sigma_e(E_e)$, $\sigma_e(\nu_e)$, and $\nu_e(E_e)$ can be obtained analytically for this incompressible case; however, they are rather complicated functionally and hence we do not explicitly give them here. Also, the cross-property map $\nu_e(E_e)$ in this case is the same as the top curve in Fig. 9 and, thus, is not shown graphically again here.

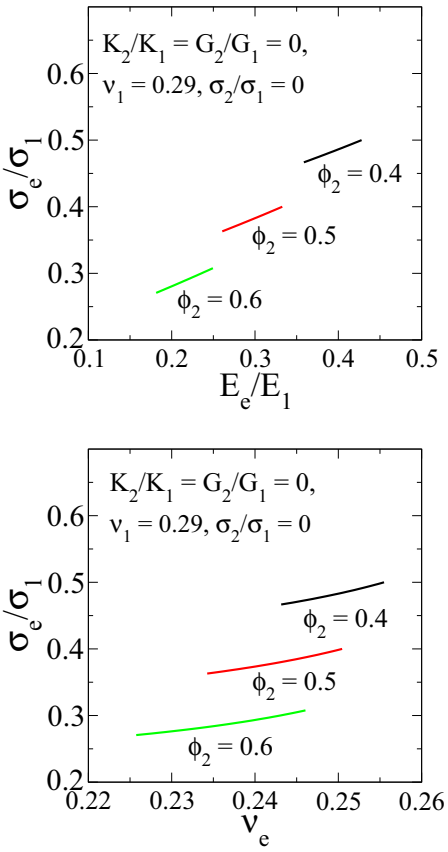

FIG. 10. Cross-property maps for $\sigma_e(E_e)$ (top) and $\sigma_e(\nu_e)$ (bottom) for compressible matrices that contain insulating cavities at select high values of the inclusion volume fraction ϕ_2. For a fixed value of ϕ_2, moving along any curve from right to left, ζ_2 increases from its minimum value of 0.

E. Compressible matrix with conducting/insulating liquid inclusions

Here we determine cross-property maps for compressible matrices ($\nu_1 < 1/2$) and liquid inclusions ($\nu_2 = 0.5$ and $G_2/G_1 = 0$) that are either superconducting ($\sigma_2/\sigma_1 = \infty$) or perfectly insulating ($\sigma_2/\sigma_1 = 0$). This is a model of a fluid-saturated porous medium.

Figure 11 shows the cross-property maps for compressible matrices with $\nu_1 = 0.29$ and superconducting liquid inclusions for inclusion volume fractions $\phi_2 = 0.4$, 0.5, and 0.6. The effective conductivity $\sigma_e(E_e)$ and effective Poisson's ratio $\nu_e(E_e)$ are monotonically decreasing functions of E_e for fixed ϕ_2, and $\sigma_e(\nu_e)$ is a monotonically increasing function of ν_e. The left end point of $\sigma_e(E_e)$ and $\nu_e(E_e)$ corresponds to the largest value of ζ_2, and the right end point of $\sigma_e(E_e)$ and $\nu_e(E_e)$ corresponds to $\zeta_2 = 0$ (Hashin-Shtrikman upper bound for E_e) for the respective ϕ_2. The left end point of $\sigma_e(\nu_e)$ corresponds to the $\zeta_2 = 0$ (Hashin-Shtrikman lower bound for σ_e), and the right end point of $\sigma_e(\nu_e)$ corresponds to the largest value of ζ_2 for the respective ϕ_2.

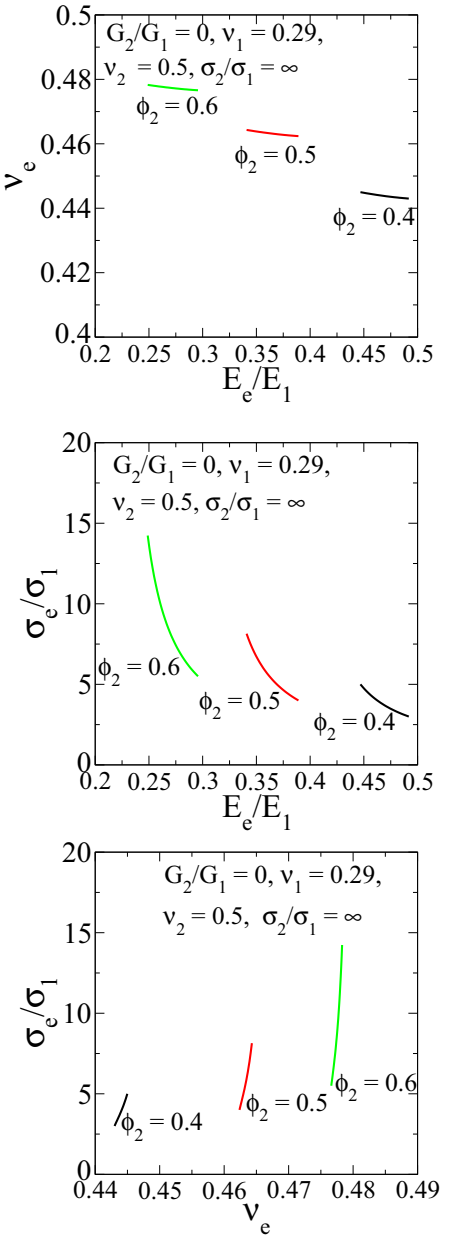

FIG. 11. Cross-property maps $\nu_e(E_e)$ (top), $\sigma_e(E_e)$ (middle), and $\sigma_e(\nu_e)$ (bottom) for compressible matrices that contain conducting liquid inclusions at select high values of the inclusion volume fraction ϕ_2. For $\nu_e(E_e)$ and $\sigma_e(E_e)$ at fixed ϕ_2, moving along a curve from right to left, ζ_2 increases from its minimum value of 0. For $\sigma_e(\nu_e)$ at fixed ϕ_2, moving along a curve from left to right, ζ_2 increases from its minimum value of 0.

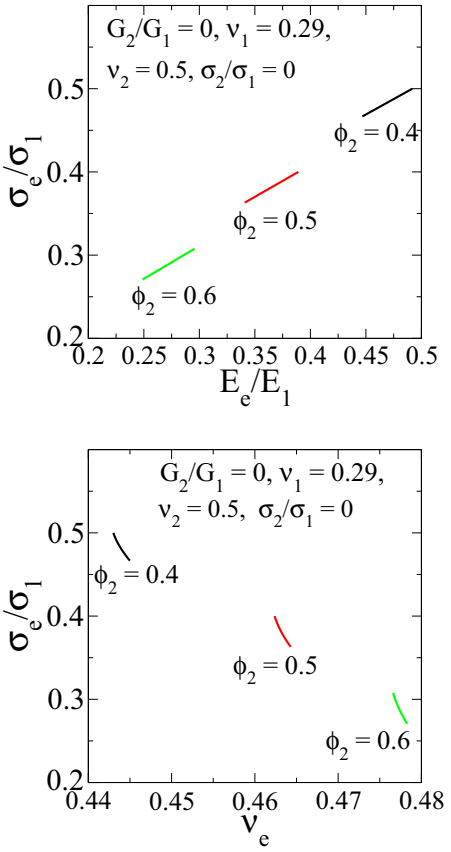

FIG. 12. Cross-property maps $\sigma_e(E_e)$ (top) and $\sigma_e(\nu_e)$ (bottom) for compressible matrices that contain insulating liquid inclusions at select high values of the inclusion volume fraction ϕ_2. For $\sigma_e(E_e)$ at fixed ϕ_2, moving along a curve from right to left, ζ_2 increases from its minimum value of 0. For $\sigma_e(\nu_e)$ at fixed ϕ_2, moving along a curve from left to right, ζ_2 increases from its minimum value of 0.

Figure 12 shows the cross-property maps $\sigma_e(E_e)$ and $\sigma_e(\nu_e)$ for compressible matrices with $\nu_1 = 0.29$ and insulating liquid inclusions for inclusion volume fractions $\phi_2 = 0.4$, 0.5, and 0.6. The cross-property map $\nu_e(E_e)$ in this case is the same as the top curve in Fig. 11 and, thus, is not shown in Fig. 12. The effective conductivity $\sigma_e(E_e)$ is a monotonically decreasing function of E_e for fixed ϕ_2, and $\sigma_e(\nu_e)$ a monotonically increasing function of ν_e. The left end point of $\sigma_e(E_e)$ corresponds to the largest value of ζ_2, and the right end point of $\sigma_e(E_e)$ corresponds to $\zeta_2 = 0$ (Hashin-Shtrikman upper bound for E_e) for the respective ϕ_2. The left end point of $\sigma_e(\nu_e)$ corresponds to the $\zeta_2 = 0$ (Hashin-Shtrikman upper bound for σ_e), and the right end point of $\sigma_e(\nu_e)$ corresponds to the largest value of ζ_2 for the respective ϕ_2.

F. Compressible matrix with conducting/insulating, auxetic inclusions

Here we determine cross-property maps for compressible matrices ($\nu_1 < 1/2$) and superrigid and auxetic inclusions ($G_2/G_1 = \infty$ and $\nu_2 = -1$) that are either superconducting ($\sigma_2/\sigma_1 = \infty$) or perfectly insulating ($\sigma_2/\sigma_1 = 0$). Auxetic materials are characterized by a negative Poisson's ratio [65–67], i.e., in contrast to common materials, they laterally dilate in response to axial stretching.

We first plot in the top panel in Fig. 13 the cross-property map $\nu_e(E_e)$ for compressible matrices with $\nu_1 = 0.29$ and superrigid inclusions for inclusion volume fractions $\phi_2 = 0.4$, 0.5, and 0.6. Note that $\nu_e(E_e)$ is independent of the conductivity contrast σ_2/σ_1. The left end point of $\nu_e(E_e)$ corresponds to the $\zeta_2 = 0$ (Hashin-Shtrikman lower bound for E_e), and the right end point of $\nu_e(E_e)$ corresponds to the largest value of ζ_2 for the respective ϕ_2. The effective Poisson's ratio $\nu_e(E_e)$

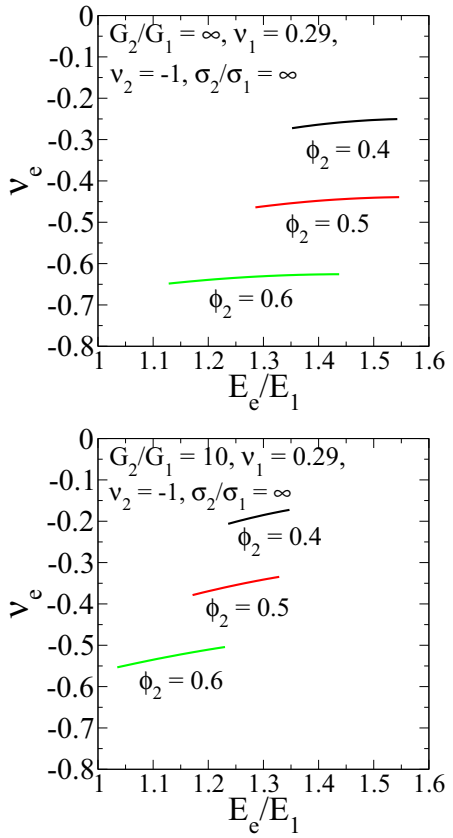

FIG. 13. Cross-property map $\nu_e(E_e)$ for compressible matrices that contain superrigid auxetic inclusions at select high values of the inclusion volume fraction ϕ_2. At a fixed value of ϕ_2, moving along any curve from left to right, ζ_2 increases from its minimum value of 0.

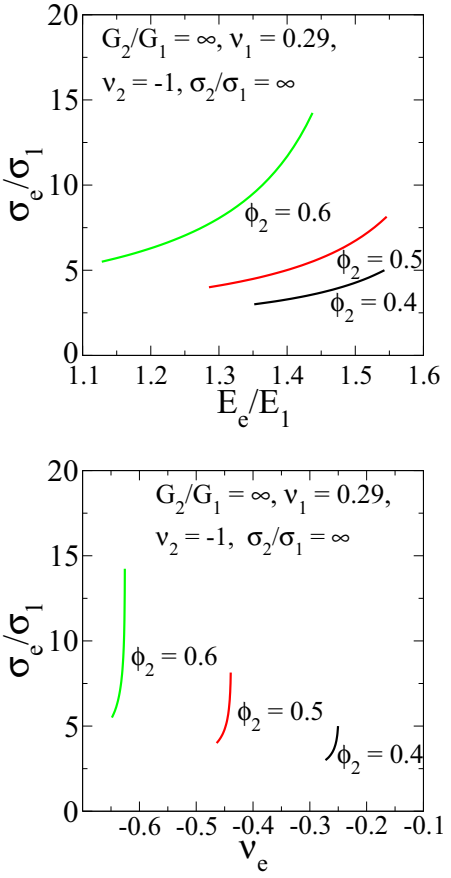

FIG. 14. Cross-property maps $\sigma_e(E_e)$ (top) and $\sigma_e(\nu_e)$ (bottom) for compressible matrices that contain conducting superrigid auxetic inclusions at select high values of the inclusion volume fraction ϕ_2. At a fixed value of ϕ_2, moving along any curve from left to right, ζ_2 increases from its minimum value of 0.

is a monotonically increasing function of E_e for fixed ϕ_2. Also, as ϕ_2 increases, ν_e becomes more negative, as expected, because the auxetic phase occupies a greater volume fraction. Moreover, all other phase contrasts being equal, changing G_2/G_1 to 10 from ∞ results in a cross-property map (bottom panel in Fig. 13) that is significantly different from the top curve shown in Fig. 13.

Figure 14 shows the cross-property maps for compressible matrices with $\nu_1 = 0.29$ and superconducting auxetic inclusions for inclusion volume fractions $\phi_2 = 0.4$, 0.5, and 0.6. The effective conductivity $\sigma_e(E_e)$ and $\sigma_e(\nu_e)$ are monotonically increasing functions of E_e and ν_e for fixed ϕ_2. The left end point for each curve corresponds to $\zeta_2 = 0$ (Hashin-Shtrikman lower bound for σ_e), and the right end point corresponds to the largest value of ζ_2 for the respective ϕ_2.

Figure 15 shows the cross-property maps for compressible matrices with $\nu_1 = 0.29$ and insulating auxetic inclusions for inclusion volume fractions $\phi_2 = 0.4$, 0.5, and 0.6. The effective conductivity $\sigma_e(E_e)$ and $\sigma_e(\nu_e)$ are monotonically decreasing functions of E_e and ν_e for fixed ϕ_2. The left end point for each curve corresponds to the $\zeta_2 = 0$ (Hashin-Shtrikman upper bound for σ_e), and the right end point corresponds to the largest value of ζ_2 for the respective ϕ_2.

IV. APPLICATION OF CROSS-PROPERTY MAPS TO THE DESIGN OF MULTIFUNCTIONAL MATERIALS

Cross-property maps can aid in the rational design of multifunctional particulate composites with specified material components and volume fractions. One first should have in mind the component materials and hence the phase properties. From a cross-property map of such phase properties, one first selects a point (pair of effective properties) on a curve for a fixed inclusion volume fraction ϕ_2. This choice implicitly determines the corresponding value of the three-point parameter ζ_2, which in turn determines the associated family of dispersions that is characterized by the spatial distribution of the inclusions and inclusion shapes and sizes. This family spans particulate composites with different degrees of order/disorder [68], which would provide experimentalists guidance in the fabrication process. Here we specifically illustrate this procedure with several examples.

To begin, suppose one wishes to design incompressible composites with rigid, conducting inclusions. This is the case depicted in the topmost panel in Fig. 4. Now imagine selecting a pair of values of the effective conductivity σ_e and Young's modulus E_e corresponding to the left end point of the curve at $\phi_2 = 0.4$, i.e., a particulate composite with $\zeta_2 = 0$. For

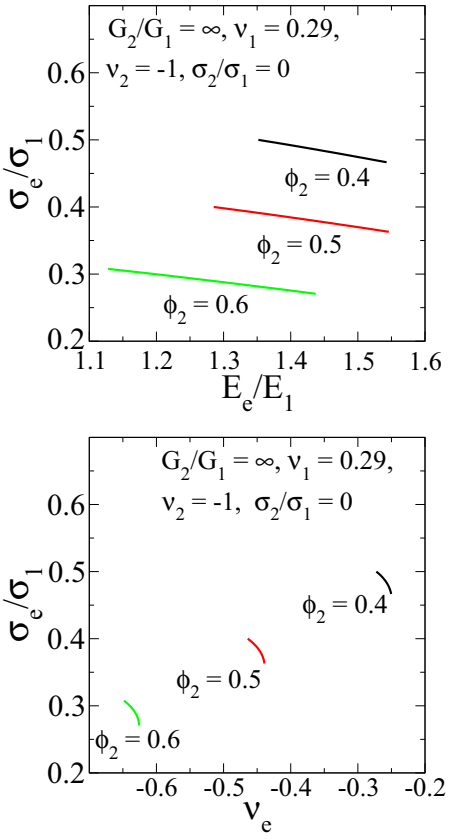

FIG. 15. Cross-property maps $\sigma_e(E_e)$ (top) and $\sigma_e(\nu_e)$ (bottom) for compressible matrices that contain insulating superrigid auxetic inclusions at select high values of the inclusion volume fraction ϕ_2. At a fixed value of ϕ_2, moving along any curve from left to right, ζ_2 increases from its minimum value of 0.

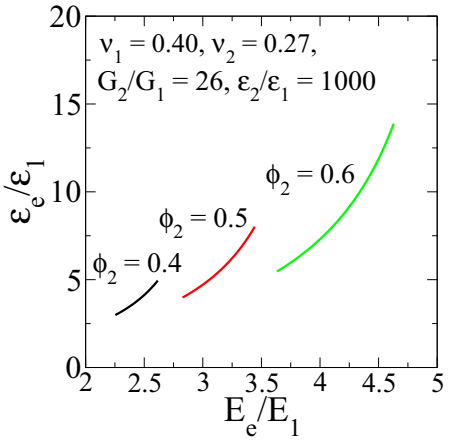

FIG. 16. Cross-property map for the effective dielectric constant $\varepsilon_e(E_e)$ for barium titanate inclusions in a polyvinyl chloride matrix at select high values of the inclusion volume fraction ϕ_2. At a fixed value of ϕ_2, moving along any curve from left to right, ζ_2 increases from its minimum value of 0.

example, such a composite, to a good approximation, could be fabricated with an elastomeric matrix [64] with spherical gold inclusions arranged on an ordered lattice, such as the fcc lattice. In Table II, one can see that ζ_2 for the fcc array at this inclusion volume fraction is relatively small, as required.

Next consider the case of a dispersion consisting of conducting superrigid, auxetic inclusions in a compressible matrix and select a pair of ν_e and E_e that corresponds to the right end point of the curve at $\phi_2 = 0.6$ in the top panel in Fig. 13, i.e., a particulate composite with $\zeta_2 = 0.33$. To a good approximation, one can fabricate this composite with nonoverlapping grooved block of metal [69] inclusions of nonspherical (e.g., ellipsoidal) shapes, which are randomly distributed in a magnesium or low-alloy carbon steel matrix [70]. As mentioned in Sec. II, dispersions of hard nonspherical inclusions possess the required sufficiently large value of ζ_2. Note that such a composite is also predicted to possess an effective conductivity $\sigma_e/\sigma_1 = 14.24$.

Finally, we now consider the case in which we purposely choose material components that have been previously employed to fabricate composites. Specifically, we consider barium titanate inclusions in a thermoplastic polymer matrix (e.g., polyvinyl chloride matrix). Such composites are used because they exhibit an effective dielectric constant up to two orders of magnitude higher than that of conventional ceramic-polymer composites [71]. We exploit the fact, as noted earlier, that the dimensionless effective conductivity σ_e/σ_1 can be replaced with the dimensionless dielectric constant $\varepsilon_e/\varepsilon_1$ in Eq. (1) and hence cross-property maps derived from it. The individual phase properties for such composites are $\nu_1 = 0.40$, $\nu_2 = 0.27$, $G_2/G_1 = 26$, and $\varepsilon_2/\varepsilon_1 = 1000$. The corresponding cross-property map $\varepsilon_e(E_e)$ is shown in Fig. 16. Let us imagine that it is desired to create such a composite with $\phi_2 = 0.5$ and select the pair of values $\varepsilon_e/\varepsilon_1 = 6.91$ and $E_e/E_1 = 3.33$, which is midway between the left and the right end points. This point corresponds to $\zeta_2 = 0.25$, which, according to Table I, could be achieved by a disordered distribution of nonoverlapping spherical barium titanate inclusions of different sizes, among other possible microstructures. We note that the resulting composite is also predicted to possess $\nu_e = 0.34$.

V. DISCUSSION

In this work, we apply closed-form analytical expressions that have previously found widespread use to estimate accurately individual effective transport or elastic properties for a diverse class of dispersions to derive corresponding cross-property maps that link combinations of pairs of these effective properties to one another. Such cross-property maps and their extensions will facilitate the rational design of particulate media with desirable multifunctional characteristics [2]. In the case of dispersions, we have shown how to design multifunctional composites. One first selects a desirable set of effective properties with a specified volume fraction ϕ_2 and individual phase properties that are dictated by the cross-property maps. This determines the corresponding value of the three-point parameter ζ_2, which in turn determines the associated family of dispersions (spatial distribution of the inclusions and inclusion shapes and sizes) and, hence, guides experimentalists on how to fabricate the composites.

Our work also has implications for the application of machine-learning and other data-driven approaches [72–74]

for materials discovery. Indeed, the recent rapid development of such computational techniques along with the emergence of advanced imaging techniques [75] provides a promising automated means of devising cross-property maps for general composite microstructures. Specifically, imaging techniques such as high-throughput x-ray tomographic microscopy [75] have made it possible to acquire large amounts of high-resolution images for a wide range of materials. These image data provide important infrastructure for the identification of structure-property relations through the use of data-driven approaches [72–74]. By combining the different identified structure-property relations and eliminating the structural components (similarly to how we eliminate ζ_2 and η_2 in this work), one can ascertain cross-property maps to design the next-generation multifunctional composite materials.

ACKNOWLEDGMENT

The authors gratefully acknowledge the support of the Air Force Office of Scientific Research Program on Mechanics of Multifunctional Materials and Microsystems under award No. FA9550-18-1-0514.

APPENDIX: THREE-POINT PARAMETERS ζ_2 AND η_2

Here we summarize some known results for the three-point parameters ζ_2 and η_2 for various disordered and ordered model microstructures as a function of the volume fraction, as excerpted from Ref. [3].

A two-phase *symmetric-cell material* (SCM) is constructed by partitioning space into cells of arbitrary shapes and sizes, with cells being randomly designated as phases 1 and 2 with probability ϕ_1 and ϕ_2, respectively [76]. Consider an isotropic SCM made up of d-dimensional ellipsoidal cells. Such space-filling cells must be randomly oriented and possess a size distribution down to the infinitesimally small. For d-dimensional ellipsoidal cells, one can express the three-point parameters in terms of the "depolarization" factors [3]. For example, for d-dimensional spherical cells, $\zeta_2 = \eta_2 = \phi_2$; for three-dimensional needlelike cells, $\zeta_2 = \eta_2 = \phi_1/4 + 3\phi_2/4$; and for three-dimensional disklike cells or two-dimensional needlelike cells, $\zeta_2 = \eta_2 = \phi_1$. For an SCM with identical cubical cells [3],

$$\zeta_2 = 0.11882\phi_1 + 0.88118\phi_2. \tag{A1}$$

In Tables I–III, we tabulate the three-point parameters for certain disordered and ordered dispersions.

TABLE I. Three-point parameter ζ_2 vs inclusion volume fraction ϕ_2 for various random dispersions of spheres: symmetric-cell material (SCM) with spherical cells [76,77], identical overlapping spheres [78], disordered identical hard spheres [79], and disordered hard spheres with a size distribution [57].

	Three-point parameter ζ_2			
ϕ_2	SCM with spherical cells	Identical overlapping spheres	Identical hard spheres	Polydisperse hard spheres
0.0	0.0	0.0	0.0	0.0
0.1	0.1	0.056	0.020	0.05
0.2	0.2	0.114	0.041	0.10
0.3	0.3	0.171	0.060	0.15
0.4	0.4	0.230	0.077	0.20
0.5	0.5	0.290	0.094	0.25
0.55	0.55	0.320	0.110	0.275
0.6	0.6	0.351	0.134	0.30
0.7	0.7	0.415		
0.8	0.8	0.483		
0.9	0.9	0.558		
0.95	0.95	0.604		
0.99	0.99	0.658		

TABLE II. Three-point parameter ζ_2 versus particle volume fraction ϕ_2 for hard spheres arranged on a simple cubic (SC) lattice, body-centered cubic (BCC) lattice, or face-centered cubic (FCC) lattice [80].

	Three-point parameter ζ_2		
ϕ_2	SC	BCC	FCC
0.10	0.0003	0.0000	0.0000
0.20	0.0050	0.0007	0.0004
0.30	0.0220	0.0031	0.0021
0.40	0.0678	0.0107	0.0078
0.45	0.1104	0.0184	0.0136
0.50	0.1738	0.0307	0.0232
0.60		0.0796	0.0619
0.66		0.1381	0.1095
0.70			0.1596
0.71			0.1756

TABLE III. Three-point parameter η_2 vs inclusion volume fraction ϕ_2 for various random dispersions of spheres: symmetric-cell material (SCM) with spherical cells [76,77], identical overlapping spheres [78,81], disordered identical hard spheres [82], and disordered hard spheres with a size distribution [57].

	Three-point parameter η_2			
ϕ_2	SCM with spherical cells	Identical overlapping spheres	Identical hard spheres	Polydisperse hard spheres
0.0	0.0	0.0	0.0	0.0
0.1	0.1	0.075	0.048	0.05
0.2	0.2	0.149	0.097	0.10
0.3	0.3	0.224	0.145	0.15
0.4	0.4	0.295	0.193	0.20
0.5	0.5	0.367	0.241	0.25
0.6	0.6	0.439	0.290	0.30
0.7	0.7	0.512		
0.8	0.8	0.583		
0.9	0.9	0.658		
0.95	0.95	0.710		
0.99	0.99	0.742		

[1] S. Torquato, S. Hyun, and A. Donev, Phys. Rev. Lett. **89**, 266601 (2002).
[2] S. Torquato, Annu. Rev. Mater. Res. **40**, 101 (2010).
[3] S. Torquato, *Random Heterogeneous Materials: Microstructure and Macroscopic Properties* (Springer-Verlag, New York, 2002).
[4] D. J. Bergman, Phys. Rep. **43**, 377 (1978).
[5] G. W. Milton, J. Appl. Phys. **52**, 5294 (1981).
[6] M. Avellaneda, A. V. Cherkaev, K. A. Lurie, and G. W. Milton, J. Appl. Phys. **63**, 4989 (1988).
[7] S. Torquato, Phys. Rev. Lett. **64**, 2644 (1990).
[8] M. Avellaneda and S. Torquato, Phys. Fluids A **3**, 2529 (1991).
[9] A. V. Cherkaev and L. V. Gibiansky, Proc. R. Soc. Edinburgh, A **122**, 93 (1992).
[10] G. W. Milton, *The Theory of Composites* (Cambridge University Press, Cambridge, UK, 2002).
[11] J. G. Berryman and G. W. Milton, J. Phys. D: Appl. Phys. **21**, 87 (1988).
[12] L. V. Gibiansky and S. Torquato, Phys. Rev. Lett. **71**, 2927 (1993).
[13] L. V. Gibiansky and S. Torquato, J. Mech. Phys. Solids **44**, 233 (1996).
[14] L. V. Gibiansky and S. Torquato, Proc. R. Soc. London A **452**, 253 (1996).
[15] L. V. Gibiansky and S. Torquato, J. Geophys. Res. **103**, 23911 (1998).
[16] I. Sevostianov and M. Kachanov, in *Advances in Applied Mechanics*, Vol. 42 (Elsevier, Amsterdam, 2009), pp. 69–252.
[17] S. Torquato, S. Hyun, and A. Donev, J. Appl. Phys. **94**, 5748 (2003).
[18] S. Torquato and A. Donev, Proc. R. Soc. London A **460**, 1849 (2004).
[19] Y. Jung and S. Torquato, Phys. Rev. E **72**, 056319 (2005).
[20] J. L. Gevertz and S. Torquato, Phys. Rev. E **80**, 011102 (2009).
[21] W. B. Russel, D. A. Saville, and W. R. Schowalter, *Colloidal Dispersions* (Cambridge University Press, Cambridge, UK, 1989).
[22] M. Sahimi, *Heterogeneous Materials I: Linear Transport and Optical Properties* (Springer-Verlag, New York, 2003).
[23] T. Zohdi, Philos. Trans. R. Soc. London A **361**, 1021 (2003).
[24] T. Zohdi, Mech. Mater. **38**, 969 (2006).
[25] F. Qin and C. Brosseau, J. Appl. Phys. **111**, 061301 (2012).
[26] G. Zhang, F. H. Stillinger, and S. Torquato, J. Chem. Phys. **145**, 244109 (2016).
[27] Y. Xu, S. Chen, P.-E. Chen, W. Xu, and Y. Jiao, Phys. Rev. E **96**, 043301 (2017).
[28] P. Tahmasebi and M. Sahimi, Granular Matter **20**, 45 (2018).
[29] D. Bruggeman, Ann. Phys. (Liepzig) **416**, 636 (1935).
[30] B. Budiansky, J. Mech. Phys. Solids **13**, 223 (1965).
[31] T. Mori and K. Tanaka, Acta Metall. **21**, 571 (1973).
[32] S. Boucher, J. Compos. Mater. **8**, 82 (1974).
[33] W. F. Brown, J. Chem. Phys. **23**, 1514 (1955).
[34] J. D. Ramshaw, J. Stat. Phys. **35**, 49 (1984).
[35] S. Torquato, J. Appl. Phys. **58**, 3790 (1985).
[36] G. W. Milton, Commun. Math. Phys. **111**, 281 (1987).
[37] A. K. Sen and S. Torquato, Phys. Rev. B **39**, 4504 (1989).
[38] S. Torquato, Phys. Rev. Lett. **79**, 681 (1997).
[39] S. Torquato, J. Mech. Phys. Solids **45**, 1421 (1997).
[40] S. Torquato, Int. J. Solids Struct. **35**, 2385 (1998).
[41] Z. Hashin and S. Shtrikman, J. Appl. Phys. **33**, 3125 (1962).
[42] Z. Hashin and S. Shtrikman, J. Mech. Phys. Solids **4**, 286 (1963).
[43] G. A. Francfort and F. Murat, Arch. Ration. Mech. Anal. **94**, 307 (1986).
[44] G. W. Milton, in *Homogenization and Effective Moduli of Materials and Media*, edited by J. L. Eriksen*et al.* (Springer-Verlag, New York, 1986).
[45] G. Wei and S. F. Edwards, Phys. Rev. E **58**, 6173 (1998).
[46] J. Segurado and J. Llorca, J. Mech. Phys. Solids **50**, 2107 (2002).
[47] A. P. Roberts and E. J. Garboczi, Proc. R. Soc. London A **458**, 1033 (2002).
[48] A. Mikdam, A. Makradi, S. Ahzi, H. Garmestani, D. S. Li, and Y. Remond, J. Mech. Phys. Solids **57**, 76 (2009).
[49] F. Gritti and G. Guiochon, J. Chromatogr. A **1218**, 3476 (2011).
[50] Y. Jiao and S. Torquato, Phys. Biol. **9**, 036009 (2012).
[51] H. Liasneuski, D. Hlushkou, S. Khirevich, A. Höltzel, U. Tallarek, and S. Torquato, J. Appl. Phys. **116**, 034904 (2014).
[52] Macroscopic anisotropy refers to an anisotropic effective property tensor. Macroscopic isotropy refers to an isotropic effective property tensor. The latter, in the case of the conduction problem, implies that the medium is characterized by a single scalar property, σ_e. Macroscopic isotropy in the case of the elasticity problem implies that the medium is characterized by two independent properties, e.g., the effective bulk modulus K_e and shear modulus G_e or the effective Young's modulus E_e and Poisson's ratio ν_e.
[53] n-point bounds are those that incorporate up to n-point correlation functions, i.e., the set $S_1^{(p)}, S_2^{(p)}, \ldots, S_n^{(p)}$.
[54] J. R. Willis, J. Mech. Phys. Solids **25**, 185 (1977).
[55] F. Lado and S. Torquato, Phys. Rev. B **33**, 3370 (1986).
[56] S. Torquato and F. Lado, Phys. Rev. B **33**, 6428 (1986).
[57] J. F. Thovert, I. C. Kim, S. Torquato, and A. Acrivos, J. Appl. Phys. **67**, 6088 (1990).
[58] M. J. Beran and J. Molyneux, Q. Appl. Math. **24**, 107 (1966).
[59] J. J. McCoy, in *Recent Advances in Engineering Sciences*, Vol. 5 (Gordon and Breach, New York, 1970).
[60] G. W. Milton, Phys. Rev. Lett. **46**, 542 (1981).
[61] G. W. Milton and N. Phan-Thien, Proc. R. Soc. London A **380**, 305 (1982).
[62] S. Torquato, Appl. Mech. Rev. **44**, 37 (1991).
[63] S. Torquato, J. Mech. Phys. Solids **46**, 1411 (1998).
[64] Y. Kim, J. Zhu, B. Yeom, M. Di Prima, X. Su, J.-G. Kim, S. J. Yoo, C. Uher, and N. A. Kotov, Nature **500**, 59 (2013).
[65] R. Lakes, Science **235**, 1038 (1987).
[66] G. W. Milton, J. Mech. Phys. Solids **40**, 1105 (1992).
[67] L. V. Gibiansky and S. Torquato, J. Mech. Phys. Solids **45**, 689 (1997).
[68] S. Torquato, J. Chem. Phys. **149**, 020901 (2018).
[69] L. Mizzi, R. Gatt, and J. N. Grima, Phys. Status Solidi B **252**, 1559 (2015).
[70] P. H. Mott and C. M. Roland, Phys. Rev. B **80**, 132104 (2009).
[71] E. P. Gorzkowski and M.-J. Pan, IEEE Trans. Ultrason. Ferroelectr. Freq. Control **56**, 1613 (2009).
[72] O. Wodo, S. Broderick, and K. Rajan, MRS Bull. **41**, 603 (2016).
[73] R. Cang, Y. Xu, S. Chen, Y. Liu, Y. Jiao, and M. Y. Ren, J. Mech. Des. **139**, 071404 (2017).
[74] N. Lubbers, T. Lookman, and K. Barros, Phys. Rev. E **96**, 052111 (2017).

[75] E. Guo, N. Chawla, T. Jing, S. Torquato, and Y. Jiao, Mater. Charact. **89**, 33 (2014).
[76] M. N. Miller, J. Math. Phys. **10**, 1988 (1969).
[77] G. W. Milton, J. Mech. Phys. Solids **30**, 177 (1982).
[78] S. Torquato, G. Stell, and J. Beasley, Int. J. Eng. Sci. **23**, 385 (1985).
[79] C. A. Miller and S. Torquato, J. Appl. Phys. **68**, 5486 (1990).
[80] R. C. McPhedran and G. W. Milton, Appl. Phys. A **26**, 207 (1981).
[81] J. G. Berryman, J. Phys. D **18**, 585 (1985).
[82] S. Torquato, F. Lado, and P. A. Smith, J. Chem. Phys. **86**, 6388 (1987).